



# Water Resources Research

## RESEARCH ARTICLE

10.1029/2019WR025412

### Key Points:

- The characterization of Earth surface topography using hypsometry is revisited
- A complementary variable termed Hölder exponent catchment area scaling is proposed
- Catchments are readily distinguished using Hölder exponent-conditioned variables

### Supporting Information:

- Supporting Information S1

### Correspondence to:

C. J. Keylock,  
c.j.keylock@lboro.ac.uk

### Citation:

Keylock, C. J., Singh, A., Passalacqua, P., & Foufoula-Georgiou, E. (2020). Hölder-conditioned hypsometry: A refinement to a classical approach for the characterization of topography. *Water Resources Research*, 56, e2019WR025412. <https://doi.org/10.1029/2019WR025412>

Received 22 APR 2019

Accepted 23 APR 2020

Accepted article online 27 APR 2020

## Hölder-Conditioned Hypsometry: A Refinement to a Classical Approach for the Characterization of Topography

Christopher J. Keylock<sup>1</sup>, Arvind Singh<sup>2</sup>, Paola Passalacqua<sup>3</sup>, and Efi Foufoula-Georgiou<sup>4</sup>

<sup>1</sup>School of Architecture, Building, and Civil Engineering, Loughborough University, Leicestershire, UK,

<sup>2</sup>Civil, Environmental, and Construction Engineering, College of Engineering and Computer Science, University of Central Florida, FL, USA, <sup>3</sup>Civil, Architectural, and Environmental Engineering, Cockrell School of Engineering, University of Texas at Austin, Austin, TX, USA, <sup>4</sup>Departments of Civil and Environmental Engineering and Earth System Science, Henry Samueli School of Engineering, University of California, Irvine, CA, USA

**Abstract** The effective characterization of topographic surfaces is a central tenet of geomorphology. Differences in land surface properties reveal variations in structural controls and the nature and efficacy of Earth-shaping processes. In this paper, we employ the Hölder exponents,  $\alpha$ , characterizing the local scaling behavior of topography and commonly used in the study of the (multi)fractal properties of landscapes and show that the joint probability distribution of the area of the terrain with a given elevation and  $\alpha$  contains a wealth of information on topographic structure. The conditional distributions of the hypsometric integrals as a function of  $\alpha$ , that is,  $I_{hyp\alpha}$ , are shown to capture this structure. A multivariate analysis reveals three metrics that summarize these conditional distributions: Strahler's original hypsometric integral, the standard deviation of the  $I_{hyp\alpha}$ , and the nature of any trend of the  $I_{hyp\alpha}$  against  $\alpha$ . An analysis of five digital elevation models (DEMs) from different regions of the United States shows that only one is truly described by the hypsometric integral (Mettman Ridge from central Oregon). In the other cases, the new metrics clearly discriminate between instances where topographic roughness is more clearly a function of elevation, as captured by the conditional variables. In a final example, we artificially sharpen the ridges and valleys of one DEM to show that while the hypsometric integral and standard deviation of  $I_{hyp\alpha}$  are invariant to the change, the trend of  $I_{hyp\alpha}$  against  $\alpha$  captures the changes in topography.

## 1. Introduction

The hypsometric (normalized area-elevation) curve and summarial hypsometric integral emerged as techniques for characterizing landscapes in the nineteenth century. The approach came to prominence in the 1950s (Strahler, 1952, 1992), when there was, for the first time, a focused effort on obtaining quantitative information about properties of the Earth's surface within geomorphology (Chorley & Kennedy, 1971; Chorley, 2008; Keylock, 2003). It has subsequently been widely adopted for a range of geomorphometric analyses. These include the analysis of the interacting controls on landscape from climate and tectonics (Lifton & Chase, 1992; Montgomery & Balco, 2001; Ohmori, 1993), the extent of glaciation within a landscape (Brozović et al., 2001), and the nature of glacial landscapes (Brocklehurst & Whipple, 2004; Furbish & Andrews, 1984), as well as coastal studies (Boon & Byrne, 1981) and cultivated landscapes (Verstraeten & Poesen, 2001). As an example, Walcott and Summerfield (2008) examined scale dependencies and the hypsometry of basins from southeast Africa, with basin size defined in terms of Horton-Strahler channel order. This region was selected due to its relatively simple geology and topography, with drainage divides that have persisted for over 100 Ma, and relatively constant rainfall. While there was no discernible relation between the hypsometric integral and basin area or basin relief, scale dependence was observed in basins of order 5 or less that spanned a region 10 to 100 km from the coast, where crustal displacement was observed. For smaller basins, positive hypsometric anomalies relative to the average case were a consequence of more resistive lithologies (sills and dykes) reducing the denudation in the middle and upper elevations and increasing the integral of the area-elevation curve. Thus, resistance was found to be an important control on hypsometry.

The importance of lithology and tectonic activity was also highlighted by Lifton and Chase (1992), who combined an analysis of hypsometry with one of topographic fractal dimension (Mandelbrot & van Ness, 1968). They examined the San Gabriel Mountains in California, where there is an east-west gradient in tectonic activity and a north-south gradient in climate. It was found that tectonic activity appeared to exert a control on hypsometry at all scales close to the mountain-piedmont junction, as well as influencing the topographic roughness as measured by the fractal dimension. At smaller scales, across the region, lithology was seen to exert a control on both hypsometry and the fractal dimension of topography.

Strahler (1964) classified hypsometric curves into different types based on their association to particular (Davisian) stages in the evolution of a landscape, although a simplistic interpretation of hypsometry was criticized by Carson and Kirkby (1972) as a consequence of equifinality in the relations between process and form. Hence, Willgoose and Hancock (1998) employed a landscape evolution model (Willgoose et al., 1991) to study hypsometry as a function of model parameters, including an exploration of the coupling between drainage network structure and hypsometry and how it drives the formation of the “toe” in hypsometric curves. More specifically, their simulations, both for a steady state and a topography in equilibrium but with declining relief, showed that as the aspect ratio of the basin decreased, any lateral constraint on the drainage network diminished, leading to a more highly branched drainage pattern that resulted in a higher toe to the hypsometric curve. Consequently, hypsometry is a useful measure of topography for both field and numerical studies, and sensitive measures of topography are something of particular interest as geomorphologists attempt to determine the impact of climatic changes on landscapes, a field where fractal dimension measures have also been employed (Outcalt & Melton, 1992).

### 1.1. Landscapes and Hölder Regularity

Since the focus in the 1980s and 1990s on a fractal dimension-based characterization of topography (Huang & Turcotte, 1989; Klinkenberg & Goodchild, 1992), reflections on the limitation of such a formalism (Evans & McLean, 1995) have resulted in a greater engagement with multifractality as a means to capture intermittency in a landscape (Gagnon et al., 2006). That the fractal dimension for a landscape is not constant is clear from field experience: imagine taking a transect of elevation measurements from a basin outlet to the drainage divide, detrending the signal and then studying its variability. The preferential action of deposition and diffusive processes in certain areas of the landscape will decrease variability, while fluvial incision into resistant lithologies, or scars from mass-movement activity, will have the converse effect. Thus, rather than considering just the limiting case of a constant fractal dimension (which may be generated by a fractional Brownian motion (Mandelbrot & van Ness, 1968)), it makes more sense to permit variability to arise in the exponents describing the surface roughness. Mathematically, one way to represent the variation of a signal at a point is by applying pointwise Hölder exponents. Indeed, Arneodo et al. (1997, p. 179) stated that “The singular behavior of functions is generally characterized by their Hölder exponent” and Kolwankar & Lévy Véhel (2002, p. 319) commenced their study by stating, “Characterizing the local regularity of functions is an important task in many areas . . . The most simple way of doing so is to consider the pointwise Hölder exponent.” As this latter quote implies, other methods to characterize regularity exist, such as the local Hölder exponent, which plays a role in the structure of oscillating signals, and has better behavior under fractional integration operations. Indeed, one means to estimate both these exponents simultaneously is via a microlocal approach that defines a manifold within a function space such that these two exponents are two specific fixed points (Keylock, 2017; Kolwankar & Lévy Véhel, 2002; Seuret & Lévy Véhel, 2003), illustrating that a continuum of measures of regularity can be considered. Thus, our choice of the pointwise Hölder exponent is related to considerations of ease of interpretation and its connection to well-known notions within geomorphology such as the (multi)fractal nature of landscapes. Replacing our choice with some other measure would not affect the primary assertion of this paper that consideration of regularity enhances conventional hypsometric analysis.

Examples of signals where the pointwise Hölder exponents vary are multifractional Brownian motion, (Peltier & Lévy Véhel, 1995), and the case where the different values for the exponents are imbricated—a true multifractal signal (Gagnon et al., 2003). Consequently, the use of the the pointwise Hölder exponent as a measure of regularity may be related to the multifractal formalism but is not necessarily so. In physics and mathematics, typical approaches to the synthesis of Hölder exponents into a multifractal formalism are based on the Legendre multifractal spectrum (Lashermes & Foufoula-Georgiou, 2007; Muzy et al., 1993), or sometimes the large deviation spectrum (Seuret, 2006), as well as a magnitude cumulants framework (Basu et al., 2007; Singh et al., 2016; Venugopal et al., 2006). In this study, we do not synthesize the results in these

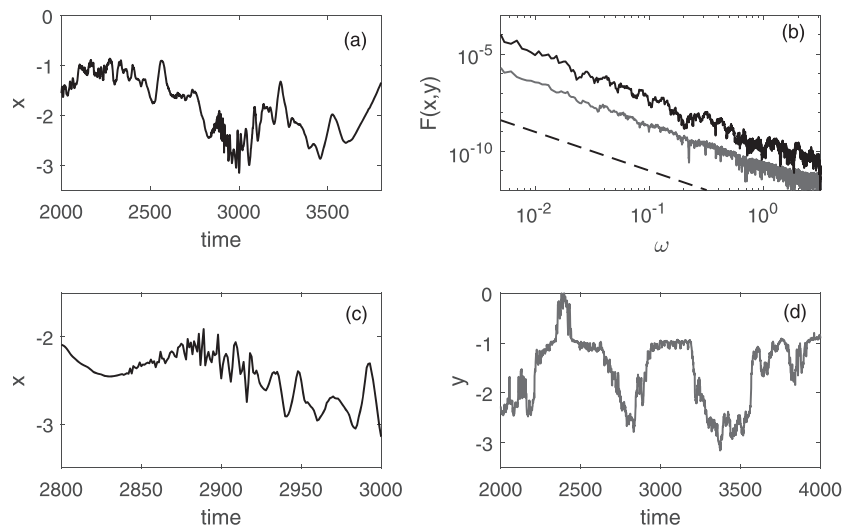


**Figure 1.** A multifractal signal is shown in (a) with its periodogram given on log-log axes by the black line in panel (b). Panel (c) shows the same signal as in panel (a) but at 10 times greater zoom. A synthetic, monofractal variant of the signal in (a) with intermittency destroyed is given in (d) as a gray line. The periodograms for this signal is shown in panel (b) by the gray line, which is displaced vertically by dividing by 100 so the two may be distinguished. The dashed line in this panel has a log-log slope of  $-2$ .

ways. Instead, we require an estimate of the pointwise Hölder exponent for each location of the digital elevation model (DEM). These results are then subsequently synthesized when integrated into an analysis of the elevation statistics. In this sense, the approach taken in this paper is similar to the velocity-intermittency approach to analyzing geophysical turbulence, where a time series of pointwise Hölder exponents is related to the velocity time series (Keylock et al., 2012, 2013). The procedure for calculating the Hölder exponents is explained in section 2.

Using an algorithm for constructing multifractal signals using a wavelet basis (Benzi et al., 1993), it is possible to obtain a multifractal signal such as that shown in Figure 1a, which clearly contains regions of high relative roughness (small Hölder exponent) as well as smoother regions (large Hölder exponent). The periodogram for this signal is given on log-log axes in panel (b) as a black line and the power law scaling to the energy in this signal is evident. Zooming in on the time series centered at time  $t \sim 2,900$  in Figure 1a gives the signal seen in Figure 1c, which is itself seen to contain rougher and smoother regions. The gray line in Figure 1b is the periodogram for a synthetic variant of this signal (Keylock, 2019; Schreiber & Schmitz, 1996) where intermittency is destroyed except by chance, and this signal is shown as a time series in Figure 1d. That this synthetic signal has the same power law scaling as the original signal indicates that both have the same fractal dimension, but the gray signal has the same fractal dimension expressed everywhere, while in the case of the intermittent, black signal, it is an average value.

Thus, it should be clear from this example that in contrast to the fractal-based approach taken in the 1990s to studying landscape elevation variability, approaches where the pointwise Hölder exponents are permitted to vary have much greater potential for characterizing the nature of terrain successfully. In recent years there have been efforts by geomorphologists to make increasing use of high-resolution topographic data by developing methods for characterizing terrain. For example, Milodowski et al. (2015) used the variability of normal vectors extracted from a quadratic function fitted to a  $3 \times 3$  kernel of elevation values (Evans, 1980) to examine topographic roughness induced by emergent bedrock as evidenced in lidar data. This approach utilized high-resolution lidar data and required a choice of the neighborhood about a given point over which the variance of the normal vectors could be determined. Such a choice could be made successfully in this case because of the focus on a specific phenomenon, although it is less clear how it could be used to characterize a whole topography. A related issue to the characterization of topography is the extraction of channel networks from digital elevation data sets. This requires considerations of channel curvatures, potentially combined with image-processing techniques (Passalacqua et al., 2010) or may also take a process-oriented view (Clubb et al., 2014).

The process-oriented approach may also be adopted for terrain characterization. For example, Grieve et al. (2016) employed an approach based on a dimensionless erosion rate,  $E^*$ , and dimensionless relief,  $R^*$ , where both terms are dependent on hillslope length and the former is also a function of hillslope curvature (Roering et al., 2007). In this approach, drainage basins are first delimited, and then discrete hillslope “patches” are defined using a connected components algorithm and form the unit for the averaging of the  $E^*$  and  $R^*$  values to extract geomorphological information. More recent work by Hurst et al. (2019) has used deviations from the  $E^* - R^*$  curve to constrain the effects of transient tectonics. Thus, there is a move to define a landscape affected by a particular suite of processes and with a particular lithology in terms of summary metrics that describe the spread of points in the  $E^* - R^*$  space, and the degree of departure from the curve for a steady-state landscape.

The approach taken in this study is rather different to those discussed above, in that we take a classical method, which was employed in a process-oriented context (Strahler used hypsometry to characterize stages of the Davisian erosion cycle) and combine it with an approach based on pointwise Hölder exponents that measure topographic roughness. The advantage of this is that (as with [multi]fractal analysis) our formalism is innately a multiscale-based approach, meaning that results are, in principle, independent of the resolution of a data product or choice of an averaging window or neighborhood provided that the resolution is sufficiently adequate for a scaling regime to be identified. This also means that we work within a framework that is consistent with formal considerations of signal regularity and smoothness, rather than the mathematically more arbitrary approaches traditionally employed in geomorphology. Clearly, an explicitly process-based approach is extremely useful for testing landscape properties with regards to particular null hypotheses, for example, steady-state evolution. By considering the statistics of terrain as a whole, rather than based on delineation into discrete geomorphic units, our formulation is complementary. In the sections below, we formalize our approach, apply it to selected DEMs for terrains in the United States, and define suitable summarial metrics of the joint distribution function for hypsometry and Hölder exponents based on an empirical analysis of these DEMs.

## 2. The Calculation of Hölder Conditioned Hypsometry

### 2.1. Dimensional Considerations

In this section, we outline the Hölder-conditioned hypsometry approach. In conventional hypsometric analysis, both the observed elevation,  $z$ , and the areas of the DEM at a given elevation,  $A(z)$ , are nondimensionalized: the former by the range of elevations in the observation region and the latter by the area of the DEM. Such nondimensionalized values are indicated by an asterisk. Hence, our elevations,  $z$ , become

$$z^* = \frac{z - z_{min}}{z_{max} - z_{min}}, \quad (1)$$

where  $z_{min}$  and  $z_{max}$  are the maximum and minimum elevations in the data set. The dimensionless catchment area,  $A^*(z^*)$  is then the proportion of the total catchment area for which the elevations correspond to an interval about  $z^*$ . With the Hölder exponents for the elevations,  $\alpha_z$ , calculated as described below, we then normalize these values in a similar fashion to the elevations:

$$\alpha^* = \frac{\alpha_z - \alpha_{min}}{\alpha_{max} - \alpha_{min}}, \quad (2)$$

where, as above,  $\alpha_{min}$  and  $\alpha_{max}$  are the maximum and minimum Hölder exponents in the data set, respectively.

### 2.2. Estimation of the Pointwise Hölder Exponents Characterizing (Multi)Fractality

For the majority of landscapes, topographic roughness is related to variation in the behavior of the first derivative of elevation as a function of distance. In this case, it is legitimate to measure the pointwise Hölder exponent according to (Venugopal et al., 2006)

$$|z(x, y) - z(x \pm \delta x, y \pm \delta x)| \sim C|\delta x|^{\alpha_z(x, y)}, \quad (3)$$

in the limit of  $|\delta x| \rightarrow 0$ , assuming a constant increment is used in the  $x$  and  $y$  directions. This yields values that are constrained such that  $0 < \alpha_z(x, y) \leq 1$ , with smoother regions corresponding to larger values for  $\alpha_z(x, y)$ . However, there is no necessary reason a priori why a flat and highly smoothed region of a landscape will not exhibit singular behavior in the higher derivatives, or why a very highly dissected landscape will not

have singular behavior in the raw elevation values. Hence, a more mathematically complete definition of the Hölder exponent is not bounded between 0 and 1. Taking this more general approach, polynomials may be used to approximate the variation of  $z$  within a local neighborhood, and the polynomial of lowest order controls the nature of the fit (Jaffard, 1997). This leads to a consideration of the differentiability of a signal (its smoothness) relative to polynomial approximations about a particular point. Simplifying for reasons of exposition to a topographic transect ( $z$  as a function of  $x$ ) and employing a Taylor series expansion gives

$$T_{x_0}(x) = \sum_{i=0}^{m-1} \frac{z^i(x)}{i!} (x_0 \pm \delta x)^i, \quad (4)$$

where  $x_0$  is a specific position and  $m$  is the number of times that  $z$  is differentiable in  $x_0 \pm \delta x$ . It then follows that  $z(x_0)$  has a pointwise Hölder exponent,  $\alpha_z \geq 0$  if a constant  $K > 0$ , and the polynomial  $T_{x_0}(x)$  of degree  $m$  exists such that

$$|z(x) - T_{x_0}(x)| \leq K|x - x_0|^\beta. \quad (5)$$

The Hölder regularity,  $\alpha_z$ , is then given by the supremum (least upper bound) of  $\beta$  that fulfills (5).

It is helpful to note the differences between this formulation and studies of multifractality in geomorphology. Veneziano and Iacobellis (1999) showed how spectral and variogram-based methods fail to differentiate between fractal and multifractal systems because of the consideration of just the second moments of the increments. They also critiqued the use of gradient amplitudes rather than increments for studying the scaling properties of topography as such an approach indicated a multifractal-like scaling even when the Hölder exponent was constant. However, their favored method based on generalized increments incorporated an averaging operation. Thus, while it is useful for characterizing the multifractal spectrum, it is not helpful for evaluating the Hölder exponent at a point. For landscapes shaped by a mixture of diffusive processes (soil creep) and fluvial incision processes, they noted that for all moment orders, plots of the elevation increments as a function of  $\delta x$  exhibited a scale break that reflected the differences in the scales dominated by diffusive and incision processes. As a consequence they recommended separating out hillslopes from drainage networks before calculating the increment statistics. In our study, we have selected the pointwise Hölder exponent, which is defined in the limit of  $\delta x \rightarrow 0$ . Hence, we will obtain a “channel-like” scaling if our location of interest  $(x, y)$  is near a channel and a “hillslope-like” scaling if it is far from a channel. Thus, we sidestep the interesting, open question raised by Veneziano and Iacobellis (1999): What is the appropriate formulation of regularity that captures the mixture of processes occurring in a landscape as  $\delta x$  varies? The final example in this study examines an artificially modified DEM to show that we can detect changes in the relative dominance of regions that are sharply incised and those that are dominated by diffusive smoothing.

Accurate estimation of Hölder exponents can be undertaken in appropriate function spaces (Keylock, 2017; Seuret & Lévy Véhel, 2003) or via refinements to the work of Jaffard (1997) on wavelet bases (Katul et al., 2001; Lashermes et al., 2007). However, a simple and rapid method (Kolwankar & Lévy Véhel, 2002) is based on a log-log regression of the signal oscillations,  $O_{x_0 \pm \delta}$ , within a distance  $\delta$  of the location of interest,  $x_0$ , against  $\delta$ , where  $O_{x_0 \pm \delta}$  is given by

$$O_{x_0 \pm \delta} = \max(z_{x \in (x_0 - \delta, \dots, x_0 + \delta)}) - \min(z_{x \in (x_0 - \delta, \dots, x_0 + \delta)}). \quad (6)$$

In a previous study we showed that this approach performs well (Keylock, 2010) and it has been used extensively in our work on characterizing flow structures in turbulent flows (e.g., Keylock et al., 2013, 2016). Thus, it is adopted in this study, based on the implementation in the Fraclab toolbox (INRIA, 2017).

### 2.3. Example Digital Elevation Model

An example DEM is used in this section to demonstrate the utility of our approach. This DEM, sampled at a resolution of 1 m, represents a 2,048 m  $\times$  2,048 m region of the Middle Fork Feather River catchment in the northern Sierra Nevada, California (Sangireddy et al., 2017). These data are available from OpenTopography (<http://www.opentopography.org>). The DEM is shown in Figure 2a, with the Hölder exponents derived from these elevation values shown in Figure 2b.

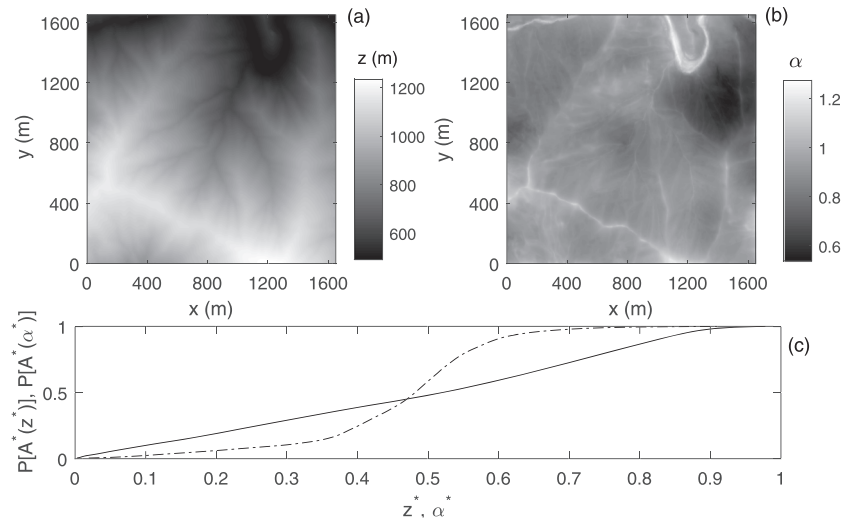


**Figure 2.** A DEM of the Middle Fork Feather River is shown in panel (a) with the accompanying Hölder exponents shown in panel (b). Panel (c) shows the classic hypsometric function (solid line) and the Hölder exponent-catchment area scaling (HECAS) (dot-dashed line).

#### 2.4. The Classic Hypsometric Function and Integral

We consider that a set of elevations,  $z$ , has been collected or interpolated onto a regular, rectangular grid with coordinates given by  $(x, y)$  and dimensions to the grid of  $X$  and  $Y$ , respectively. Having standardized the elevations, the area,  $A^*$ , associated with a given elevation band is then given simply by counting the number of values arising in that band. Thus, with  $i = 1, \dots, N_z$  elevation bands,  $z_j^* \leq \tilde{z}_i^* < z_{j+1}^*$ , the empirical probability for  $A^*$  as a function of  $\tilde{z}_i^*$  may be written as

$$p[A^*(z^*)] = \frac{A(\tilde{z}^*(i))}{X \times Y}. \quad (7)$$

The distribution of these probabilities,  $P[A^*(z^*)]$ , gives the standard hypsometric curve (Strahler, 1952), where  $P[\dots]$  indicates a cumulative distribution function. The hypsometric integral is then, in the limit of  $N_z \rightarrow \infty$ , given by

$$I_{hyp} = \int_{z^*=0}^{z^*=1} P[A^*(z^*)] dz^*. \quad (8)$$

The solid line in Figure 2c shows the hypsometric function for Feather River, which has an integral of  $I_{hyp} = 0.510$ , which according to Strahler (1964) is a typical value for a “mature” landscape.

As a practical point, in this study we do not form the  $\tilde{z}^*$  bands by dividing the  $z^*$  values into  $N_z$  equal intervals but instead divide into equal quantiles of  $z^*$ , so that each band contains the same area. This is to provide more robust evaluation of the joint distribution function (defined below) as we can choose the discretization based on a constant density for each marginal variable.

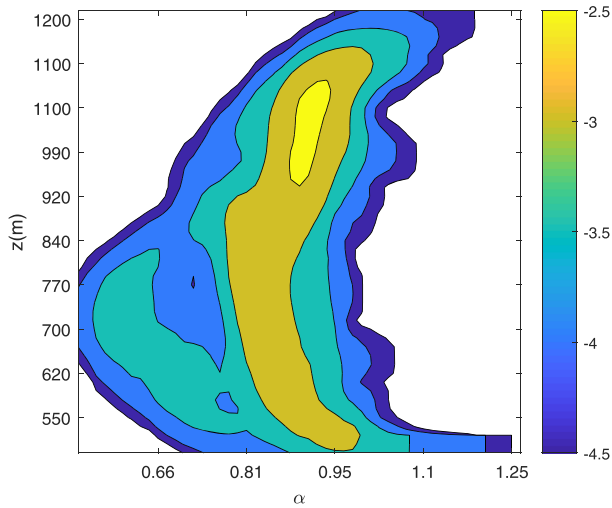
#### 2.5. Hölder Exponent-Catchment Area Scaling

In a directly analogous manner to the discussion in the previous section, we can obtain the Hölder exponent-catchment area scaling (HECAS) from our Hölder map. That is, a pointwise Hölder exponent has been calculated for every position in the DEM so that we have information on the local scaling behavior of the topography (the fractal dimension at that position). Denoting this field by  $\alpha_z(x, y)$ , then similar to  $z(x, y)$  in the previous section, we can discretize the ordered list of these values into  $i = 1, \dots, N_\alpha$  discrete bands,  $\alpha_j^* \leq \tilde{\alpha}_i^* < \alpha_{j+1}^*$ . The probability for  $A^*$  as a function of  $\tilde{\alpha}_i^*$  is

$$p[A^*(\alpha^*)] = \frac{A(\tilde{\alpha}^*(i))}{X \times Y}, \quad (9)$$

and cumulative distribution function is  $P[A^*(\alpha^*)]$ . The integral of this curve in the limit of  $N_\alpha \rightarrow \infty$  is

$$I_{\alpha^*} = \int_{\tilde{\alpha}^*=0}^{\tilde{\alpha}^*=1} P[A^*(\alpha^*)] d\tilde{\alpha}^*. \quad (10)$$



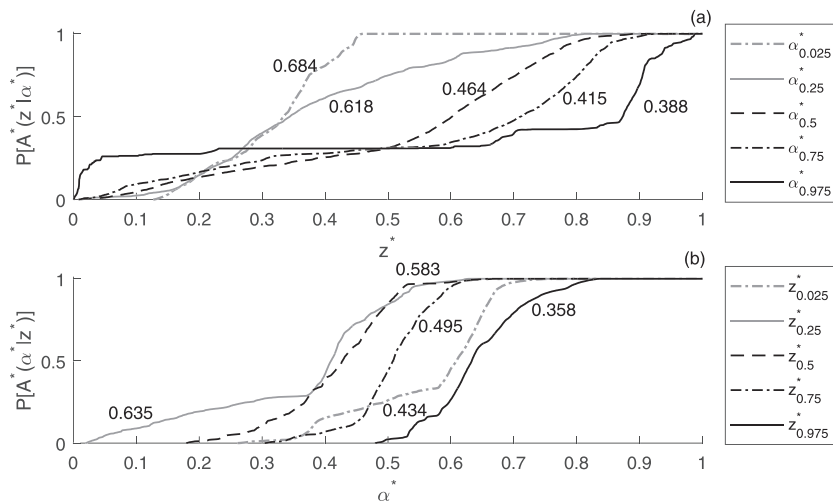
**Figure 3.** The joint probability distribution function,  $p[A^*(z, \alpha)]$  for Feather River shown as a contour map with probability contours distributed logarithmically and ranging from  $10^{-4.5}$  to  $10^{-2.5}$ .

Figure 2c shows the HECAS for the Feather River catchment (dot-dashed line), which has an integral of  $I_{\alpha^*} = 0.538$ .

### 2.6. Hölder-Conditioned Hypsometry

The two functions shown in Figure 2c are the cumulated marginal distributions for  $A^*$ . Hence, the starting point for deriving the Hölder-conditioned hypsometry is the joint probability distribution function (JPDF) for  $A^*$ , or  $p[A^*(z^*, \alpha^*)]$ , which is shown in Figure 3, although with axis labels for  $z$  and  $\alpha$  rather than their normalized variants; that is, it is  $p[A^*(z, \alpha)]$  that is shown. This JPDF contains a wealth of information on the structure of the terrain, including the anticipated “crescent-like” shape that highlights that the regions of smoothest topography occur at both the greatest (drainage divides) and smallest (river channel and floodplain) elevations. This non-Gaussian shape to the JPDF highlights the issue with using average values for each axis (i.e.,  $I_{\alpha^*}$  and  $I_{hyp}$ ) to characterize the shape of the JPDF: The center of mass of a crescent lies outside the regions containing the bulk of the density. In addition, this shape is more complex than being simply crescent-like as there is a separate mode to the distribution at  $(600 < z < 800 \text{ m}, \alpha < 0.66)$ , highlighting that within the lower third of the elevation range, there are the regions of greatest terrain roughness.

From this joint distribution, we may extract a conditional hypsometric function by cumulating the values of  $p[A^*(z^*, \alpha^*)]$  for a given choice of  $\alpha$  (i.e., cumulating along a particular vertical transect imposed on Figure 3 and suitable renormalizing to give  $P[A^*(z^* | \alpha^*)]$ ). This may be contrasted with integrating out the  $\alpha$  axis and cumulating, which would lead to the marginal distribution—Strahler’s conventional  $P[A^*(z^*)]$ . Five example Hölder-conditioned hypsometry functions are shown in Figure 4a for values of  $\alpha^*$  that span those that occur in this DEM from the 2.5 percentile to the 97.5 percentile. The bimodal nature of the hypsometry for  $\alpha^* = 0.975$  is consistent with the crescent shape of the JPDF seen in Figure 3 and is explicit here, as shown by the black, solid line. This attains 25% from the smallest 2.5% of elevations, is approximately flat until  $z^* = 0.87$ , and then acquires the final 55% of its mass in the upper 13% of elevations. In marked contrast are the results for  $\alpha^* = 0.025$  shown as a gray, dash dotted line, with 100% of its mass for  $0.15 < z^* < 0.45$ : High roughness values are not found in the very lowest elevations of the DEM and are exhausted by the mid-elevations.



**Figure 4.** The Hölder-conditioned hypsometry for Feather River at five choices of  $\alpha^*$  is shown in panel (a). The hypsometric integrals for each of these curves,  $I_{hyp|\alpha^*}$ , are stated next to each line. Panel (b) provides the conditional Hölder exponent-catchment area scaling function, for five corresponding choices of  $z^*$ . The values for  $I_{\alpha^*|z^*}$  are stated next to each line.

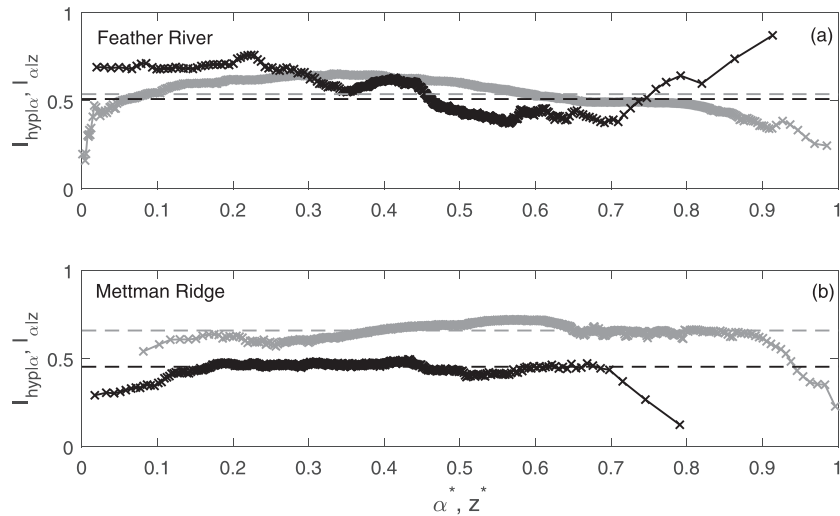


**Figure 5.** The Hölder conditioned hypsometry profile (black) and elevation-conditioned Hölder scaling profile (gray) for the Feather River (a) and Mettman Ridge (b). The black and gray dashed lines show the values for  $I_{hyp|\alpha^*}$  and  $I_{\alpha^*|z^*}$ , respectively.

The hypsometric integrals for each of these Hölder conditioned hypsometries, that is  $I_{hyp|\alpha^*}$ , are stated next to each curve. None of the values quoted, including that for  $\alpha^* = 0.5$ , are that close to  $I_{hyp}$ , supporting the hypothesis that provides the rationale for this paper: Information on the (multi)fractal structure of landscapes is a useful complement to standard hypsometric analysis.

Given the joint distribution function in Figure 3, we do not, of course, have to follow the logic of Strahler's approach; we can also obtain  $P[A^*(\alpha^*|z^*)]$ , by cumulating along a horizontal transect in this figure and suitably renormalizing. Thus, we can also examine how the Hölder exponent-catchment area scaling varies with  $z^*$ , with example functions shown in Figure 4b. There is an obvious qualitative difference here in that, while in Figure 4a,  $I_{hyp|\alpha^*}$  decreases as  $\alpha^*$  increases, in this panel we see that the two smallest values for  $I_{\alpha^*|z^*}$  arise for  $z^* = 0.025$  (gray, dot-dashed line) and  $z^* = 0.975$  (black, solid line). These two curves are rather different in nature, however, with the former exhibiting bimodality (low elevations have both low and high Hölder exponents, representing the footslopes and the valley floor, respectively), while at high elevations, nearly all the  $\alpha^*$  values are in the upper half of the distribution (smoother surfaces). In addition, the curve for  $z^* = 0.25$  (gray line) contains the lowest  $\alpha^*$  values and reflects the separate mode to the joint distribution discussed above.

### 3. Summary Measures

Having extended the original hypsometric function to two forms of conditional analysis (the cumulative distribution of areas as a function of elevation for a given  $\alpha$  and the cumulative distribution of areas as a function of Hölder exponent for a given  $z$ ), we need to form summarial measures for the family of curves we have derived in each case. In the spirit of Strahler's original formulation, the appropriate way to summarize all such curves shown in Figure 4 is via their integrals (the labels next to each line). We may then plot  $I_{hyp|\alpha^*}$  for all  $\alpha^*$  and  $I_{\alpha^*|z^*}$  for all  $z^*$ . These profiles are shown in Figure 5a for the Feather River with estimation undertaken at 500 different values for  $\alpha^*$  and  $z^*$ . That the values do not span the full support of the abscissa is because each value is the median for each equal quantile and there is very little catchment area in the uppermost elevations, in particular.

For comparative purposes, similar plots are given for the data from a  $1,024 \times 1,024$  m DEM extracted for the Mettman Ridge area of central Oregon, also studied by Sangireddy et al. (2017). The mean value for  $I_{hyp|\alpha^*}$  for these two cases (i.e., the value for  $I_{hyp}$ ) is greater for Feather River ( $I_{hyp} = 0.510$ ) than for Mettman Ridge ( $I_{hyp} = 0.453$ ), with the respective value of  $I_{\alpha^*} = 0.659$  for Mettman Ridge greater than that for Feather River ( $I_{\alpha^*} = 0.538$ ). Thus, the tendency for Feather River to have a greater proportion of its area at lower elevations (greater  $I_{hyp}$ ) leads to a tendency to have a greater proportion of its area associated with reduced roughness (lower value for  $I_{\alpha^*}$ ). Hence, while the “crescent” shape of the joint distribution function in Figure 3 indicates

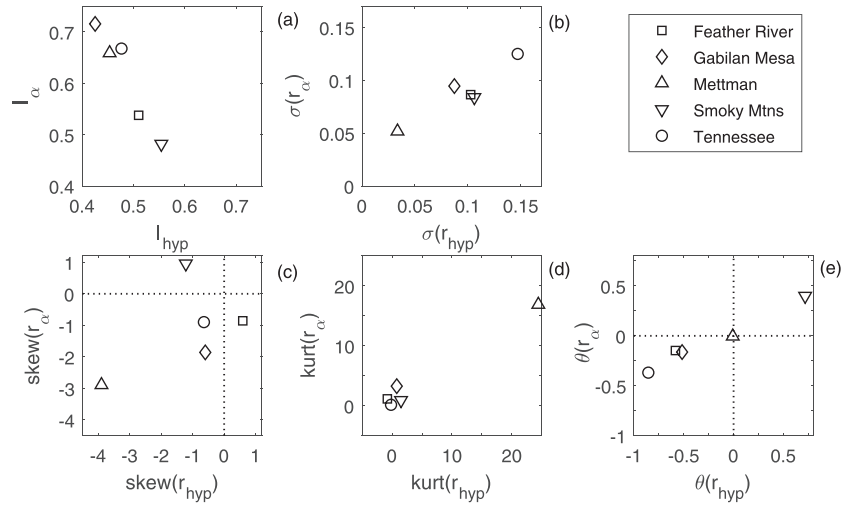


**Figure 6.** The primary indices,  $I_{hyp}$  and  $I_{\alpha^*}$  (a) together with the moments of residuals (b)-(d) and residual slopes (e) for five DEMs extracted from those studied by Sangireddy et al. (2017). The kurtosis is defined such that the value for a Gaussian distribution is 0.0.

that smooth regions arise at both high and low elevations, the dominant effect when comparing these two catchments is for the low elevation state to dominate, in accord with the distribution of the mass of the joint distribution. Geomorphologically, this means that the smoothing effect of deposition at low elevations dominates (in terms of proportion of catchment area) over the diffusive nature of processes such as rain splash on drainage divides and summit plateaux.

When examining Figure 5, it is also clear that there is much more information contained in our conditional profiles than just the mean values, and these provide more detail on how one may discriminate between catchment characteristics. For example, as already demonstrated qualitatively in Figure 4a, but shown comprehensively in Figure 5a, the majority of the  $I_{hyp|\alpha^*}$  values for Feather River differ greatly from their average value,  $I_{hyp}$ , and the negative trend to these values for  $I_{hyp|\alpha^*}$  as a function of  $\alpha^*$  we previously detected is also very clear for  $0.2 < \alpha^* < 0.7$ . Hence, in this case, it is insufficient to solely use the Strahler hypsometric integral to characterize this landscape because of the large variability and significant trend to the  $I_{hyp|\alpha^*}$  values. In addition, with the exception of the  $0.6 < z^* < 0.8$  region, there are also differences between the  $I_{\alpha^*|z^*}$  values and their average,  $I_{\alpha^*}$ .

In contrast, the Mettman Ridge profiles are essentially identical to the overall integrals,  $I_{hyp}$  and  $I_{\alpha^*}$ , over nearly the full range of values. Hence, while the Strahler hypsometric integral seems to capture a true property of the Mettman Ridge topography as values for  $I_{hyp|\alpha^*}$  are close to  $I_{hyp}$  for most  $\alpha^*$ , for the Feather River DEM the hypsometric integral is merely the first statistical moment of a more complex phenomenon that requires characterization by higher order measures.

One efficient way to quantify this variation is in terms of the residuals, that is,

$$\begin{aligned} r_{\alpha} &= I_{\alpha^*|z^*} - I_{\alpha^*}, \\ r_{hyp} &= I_{hyp|z^*} - I_{hyp}, \end{aligned} \quad (11)$$

the distance of each point in Figure 5 from its mean (dashed lines). Similar to residual analysis when examining quality of fit of a least squares regression line, one may then consider the statistical moments of these residuals, as well as any trend. Thus, we consider five potential summary metrics for hypsometry and HECAS: (i) the overall integrals,  $I_{hyp}$  and  $I_{\alpha^*}$ ; (ii) the standard deviation of the residuals,  $\sigma(r_{hyp})$  and  $\sigma(r_{\alpha})$ ; (iii) the residual skewness,  $skew(r_{hyp})$  and  $skew(r_{\alpha})$ ; (iv) the kurtosis of the residuals with the value of 3 for a Gaussian distribution subtracted,  $kurt(r_{hyp})$  and  $kurt(r_{\alpha})$ ; and (v) the slopes,  $\theta(r_{hyp})$  and  $\theta(r_{\alpha})$ , of the best fit straight line to  $I_{hyp|\alpha^*}$  versus  $\alpha^*$ , and  $I_{\alpha^*|z^*}$  vs  $z^*$ , respectively.

The values for each of these terrain measures for DEMs extracted from the regions studied by Sangireddy et al. (2017) are shown in Figure 6. It is clear that there is a strong negative correlation between  $I_{hyp}$  and  $I_{\alpha^*}$ , and strong positive correlations between  $\sigma(r_{hyp})$  and  $\sigma(r_{\alpha})$ , as well as  $\theta(r_{hyp})$  and  $\theta(r_{\alpha})$ . The catchment

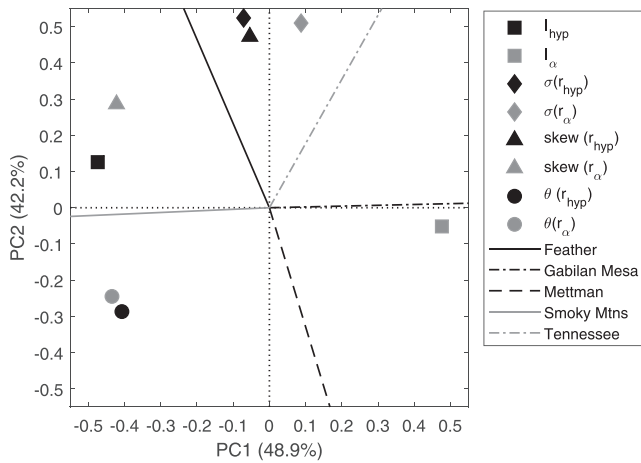


**Figure 7.** The loading of the eight original measures in the space of the leading two principal components (PC1 and PC2), with black symbols indicating hypsometric-based methods and gray Hölder-based methods. The lines indicate the direction of the weighting for each of the catchments studied.

principal components explain 91% of the total variance. It is clear that the two measures that discriminate the data best on the leading component (48.9% of the total variance) are  $I_{hyp}$  and  $I_{\alpha}$ , supporting the use of standard hypsometric analysis. The two terms that are extremal on the second component are  $\sigma(r_{hyp})$  and  $\theta(r_{hyp})$ . As well as the negative correlation between these two measures, the positive correlations between the two types of  $\sigma(\dots)$  and two types of  $\theta(\dots)$  seen in the bivariate analysis in Figures 6b and 6e are also clear. However, the advantage of the multivariate approach is that it becomes clear that while the two skewness measures are not correlated to each other,  $skew(r_{hyp})$  is closely related to  $\sigma(r_{hyp})$ , and  $skew(r_{\alpha})$  is somewhat associated with  $I_{hyp}$ . Thus, given the choice to follow the convention established by Strahler (1952) and make use of  $I_{hyp}$  rather than  $I_{\alpha}$ , Figure 7 implies that the best additional measures to characterize the DEMs are  $\sigma(r_{hyp})$  and  $\theta(r_{hyp})$ . This also has the advantage that all three measures are explicitly about the hypsometry, with the Hölder exponents acting as a conditioning variable only. An attempt to reduce analysis to a more restricted subset of the original variables would imply the use of  $I_{hyp}$  and  $\sigma(r_{hyp})$  for a bivariate analysis directly relatable to conventional hypsometry, or either  $\theta(r_{hyp})$  or  $skew(r_{\alpha})$  for univariate analysis.

#### 4. Discussion of the Hölder-Conditioned Hypsometric Triplet

Clearly, there is a wealth of information in the JPFD shown in Figure 3, but the three selected summary measures extract pertinent features of the landscape structure as shown in Figure 8. In Strahler's original conceptualization of landscape evolution,  $0.4 \leq I_{hyp} \leq 0.6$  was deemed the range of observed values for “mature” topography (Strahler, 1964), and all our values lie within this range. Thus, that we are able to observe differences in Figure 8 supports the rationale for this paper: Hölder-conditioned hypsometry provides additional information on the nature of landscape topography.

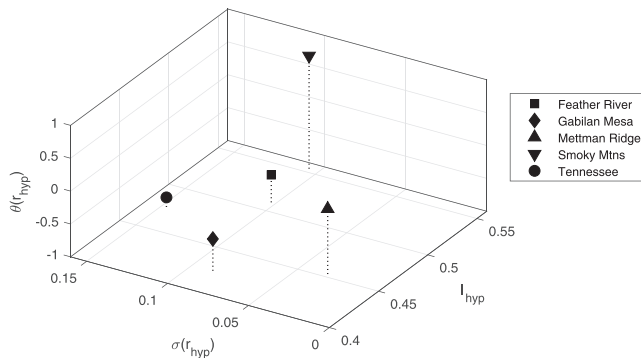


**Figure 8.** The locations of the five catchments studied by Sangireddy et al. (2017) in a three-dimensional space formed from our selected measures of hypsometry:  $I_{hyp}$ ,  $\sigma(r_{hyp})$  and  $\theta(r_{hyp})$ .

with the lowest variances for both profiles is Mettman Ridge, shown in Figure 5b. In other words, the earlier observation that this DEM is described effectively by  $I_{hyp}$  and  $I_{\alpha}$  is more true than for any other of these five DEMs. The consequence of such a high proportion of values lying close to the mean is that when deviations from  $I_{hyp}$  and  $I_{\alpha}$  do arise for  $I_{hyp|\alpha^*}$  and  $I_{\alpha^*|z^*}$ , respectively, they result in a very high kurtosis. Thus, the kurtosis seems to have limited explanatory power compared to the lower order moments. The two skewnesses are the least-correlated pair of moments and therefore discriminate between the catchments the most effectively in a univariate sense, with Feather River the catchment with  $skew(r_{hyp}) > 0$ , the Smoky Mountains the case with  $skew(r_{\alpha}) > 0$ , and the other three DEMs exhibiting negative skewness for both measures.

In order to determine which of the measures best characterize the variability in a multivariate sense, a correlation-based principal components analysis (PCA) or proper orthogonal decomposition was undertaken using the measures in Figure 6, with the exception of the kurtosis (Figure 6d), where the strong positive skew to the values biases the linear analysis. As the extreme here (Mettman Ridge) is predictable based on the variance results, leaving out the two kurtosis measures seems justified. The results of the PCA are shown in Figure 7, where the two leading

As already noted, it is clear that Mettmann Ridge is the DEM that is most closely represented by  $I_{hyp}$  as indicated by its near zero value for  $\sigma(r_{hyp})$ . This is also supported by the absence of a significant slope to the relation between  $I_{hyp|\alpha^*}$  and  $\alpha^*$ , with  $\theta(r_{hyp}) = -0.01$  for this DEM. There are particularly large magnitude values for  $\theta(r_{hyp})$  for the Tennessee Valley,  $\theta(r_{hyp}) = -0.85$ , and the Smoky Mountains,  $\theta(r_{hyp}) = 0.72$ . That these slopes are opposite in sense demonstrates the range of behavior observed in natural topographies. In the Tennessee valley, the catchment area associated with the topographically rough parts of the catchment is associated with the lower elevations, with the low hypsometric integral for the smoothest parts of the catchment highlighting the relatively

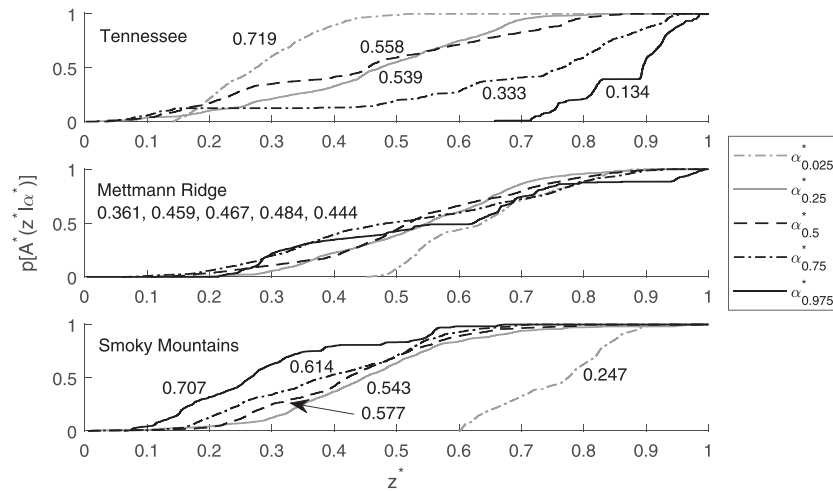


**Figure 9.** The Hölder-conditioned hypsometry for the Tennessee Valley (top), Mettmann Ridge (middle), and Smoky Mountains (bottom) DEMs at five choices of  $\alpha^*$ . The hypsometric integrals for each of these curves,  $I_{hyp|\alpha^*}$ , are stated next to each line for the top and bottom panels; for Mettmann Ridge they are stated in ascending order of  $\alpha^*$ . As seen in Figure 8, the panels are ordered such that  $\theta(r_{hyp})$  increases from top to bottom.

smooth nature of the upper-most elevations. The positive value of  $\theta(r_{hyp})$  for the Smoky Mountains indicates that the smooth parts of the terrain are associated with depositional valley floors and basins, with the drainage divides still relatively highly dissected. Greater detail on the Hölder-conditioned hypsometry for these two DEMs, and Mettmann Ridge, is provided in Figure 9, while the visualization of these DEMs, which is reproduced in the supporting information, support this process-based interpretation qualitatively.

The relation between landscape hypsometry and drainage network structure is an important one. Early work on slope profiles (Kirkby, 1971) established that the concave downward nature of the profile close to the divide is a consequence of diffusive (slope-dependent processes), with the upward concave regions closer to the catchment outlet require an advective process to be operating. However, as noted by Willgoose and Hancock (1998), in order to develop the “toe” to the hypsometric curve seen in Strahler’s characterization of a mature topography, it is necessary to study a two-dimensional landscape. In particular, this toe is a consequence of the role of side tributaries and, thus, network topology. At positions furthest downstream, there are fewer low-order channels dissecting the landscape, and, thus, there is an increasing contribution to the total area at or below that elevation from steep slopes, inducing a rapid change in the hypsometry. This observation resulted in the suggestion by Willgoose (1994) that hypsometry may be a sensitive indicator of channel form. Given the contrasting results in Figure 8, we can go further and suggest that the Hölder-conditioned hypsometry, potentially summarized by  $I_{hyp}-\sigma(r_{hyp})-\theta(r_{hyp})$  triplets will be a more sensitive indicator of drainage network structure for landscapes controlled by otherwise identical boundary conditions.

#### 4.1. Artificial Modification to a Catchment

In order to demonstrate the efficacy of our approach, we use an artificial test where alterations to the landscape are relatively minor, and they are dominated by changes to the Hölder exponents rather than the hypsometry. Thus, given the choice to place primacy on the hypsometry as discussed in the previous section, detection of such changes should be relatively difficult. Furthermore, because of the renormalization given in equations (1) and (2), if the original and modified DEMs are treated independently, changes to the range of  $z$  or  $\alpha_z$  values will not be detected, placing focus on the shape of the changes introduced. In this example, we use the Smoky Mountains DEM and apply to it a diffusion operator such that

$$\mathbf{Z}_t = c(x, y, t)\nabla^2\mathbf{Z} + \nabla c(x, y, t) \cdot \nabla\mathbf{Z}, \quad (12)$$

where  $c$  is a coefficient (if this is invariant the last term on the right-hand side is dropped) and  $\mathbf{Z}(x, y, t)$  is the evolution of the set of elevations that constitute the DEM over time. With  $c$  a function of the gradients in the DEM, one has that

$$c(x, y, t) = \tau\|\nabla\mathbf{Z}\|, \quad (13)$$

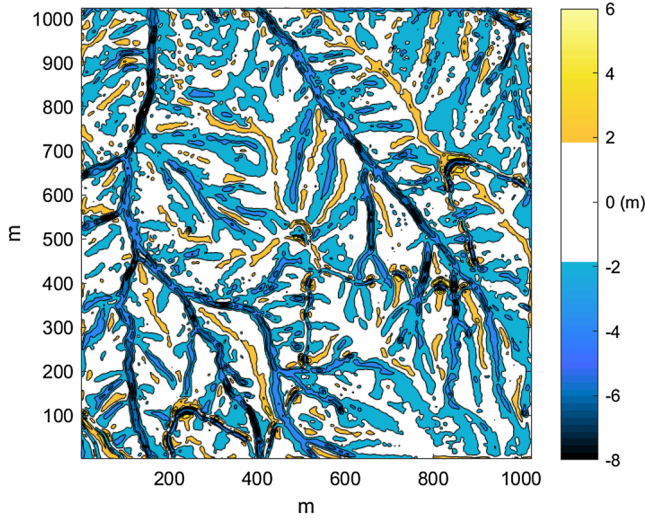


**Figure 10.** The DEM of difference between the modified DEM and the original Smoky Mountains DEM. The range of elevations in the original DEM was 405 m, and the greatest observed change was  $-8.8$  m.

and we used  $\tau = \exp(-(|\nabla Z|/K)^2)$  to produce a diffusion coefficient that is anisotropic because it is a function of magnitude of the elevation gradient in a particular direction. As a consequence, mass in the DEM is shifted toward the regions of strong local curvature, enhancing the valleys and the ridges in the DEM (Passalacqua et al., 2010; Perona & Malik, 1990).

Figure 10 shows the difference between the artificially modified surface and the original DEM. The mean difference in the DEMs was  $-9$  mm and the mean absolute difference was 1.2 m or 0.3% of the elevation range in the original DEM. However, it is clear in this figure that some valleys are eroded by as much as  $-8.8$  m, and some ridge crests increase their relative prominence by 6 m. In contrast, the impact of this sharpening of the topography was much greater for the  $\alpha$  values, with a mean change of  $-0.03$  and a mean absolute change of 0.037, which equates to 6% of the total variation in the original  $\alpha$  map.

As a consequence of the small changes to elevation, the values for  $I_{hyp}$  given in Figures 11a and 11b for the two DEMs are identical, and there is no real discernible difference in the hypsometric curves. Thus, while Strahler's original formulation is useful for understanding the long-term evolution of landscapes, it is less effective at characterizing smaller magnitude changes that might reflect base level changes due to sea level rise

or changes in precipitation regime. In contrast, and not surprisingly given the test was designed in this way, there is a measurable change in  $I_\alpha$  and a change in shape to the HECAS (shown by the gray line in the upper panels), with approximately the first 60% of Hölder exponents arising in the first 75% of the catchment area for the Smoky Mountains data and this reducing to approximately 55% for the modified topography. In terms of the conditional measure,  $I_{hyp|\alpha}$  shown as a black line in Figures 11c and 11d, while our modifications are not sufficient to change the standard deviation of these values, there is a change in the slope of the trend,  $\theta(r_{hyp})$ , which has steepened by 23% as the smoother regions at lower elevations have become even smoother relatively because of the greater roughness in the rest of the catchment. An inspection of the two  $I_{hyp|\alpha}$  functions also shows that the original data lie close to the overall integral,  $I_{hyp}$  given by the black, dashed line, for about 20% of the range of  $\alpha$  values in Figure 11c, but the modifications to the topography reduce this “flat region” in the plot to about half of its original length. Hence, the dissection reduces the range of  $\alpha$  values

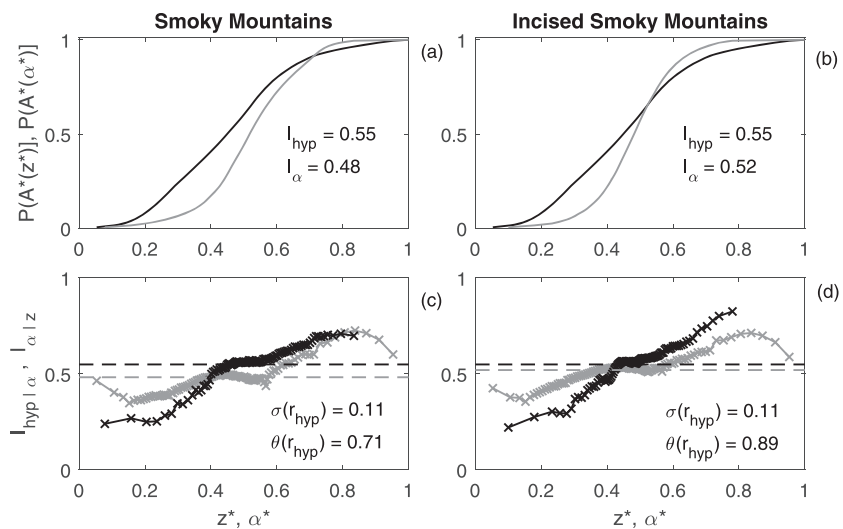


**Figure 11.** A comparison between the hypsometric properties for the original Smoky Mountains data (left-hand panels) and the artificially incised variant (right-hand panels). In each column, the upper panel shows the hypsometric function in black and the Hölder-exponent catchment area scaling (HECAS) in gray. In the lower panels the Hölder-conditioned hypsometry profile (black) and the elevation-conditioned Hölder scaling profile in gray are shown. The black and gray dashed lines in the lower panels show the values for  $I_{hyp}$  and  $I_\alpha$ , respectively, and these values are quoted in the upper panels.

for which  $I_{hyp}$  is genuinely representative. Hence, this idealized example demonstrates the extra sensitivity of the joint elevation and Hölder exponent formalism for studying topographic change as a function of changing forcings.

#### 4.2. Hypsometry and Tokunaga Cyclicity

Given that Horton-Strahler channel ordering (Strahler, 1957) is insensitive to channels of order less than  $i$  combining with another channel of order  $i$ , it has been suggested that a more appropriate network topological method is the Tokunaga cyclicity (Peckham, 1995; Tarboton, 1996; Tokunaga, 1978). For a river basin with Horton-Strahler order  $\Omega$ ,  $\tau_{ij}^{(\ell)}$  is the number of channels of order  $i$  that join the  $\ell$ th channel of order  $j$ , where  $1 \leq i < j \leq \Omega$  and  $1 \leq \ell \leq N_j$ . With  $N_{ij} = \sum_{\ell} \tau_{ij}^{(\ell)}$  the total number of channels of order  $i$  that join a channel of order  $j$ , the Tokunaga index  $T_{ij} = N_{ij}/N_j$  is the average number of channels of order  $i$  joining order  $j$  per number of order  $j$  channels. A network that is Tokunaga self-similar has the same side branch structure for all channels of a given  $j$  (i.e.,  $\tau_{ij}^{(\ell)} = T_{ij}$ ), and this is invariant with  $j$ . However, as  $j$  increases by 1, there is a need to consider new statistics,  $T_{ij}$ . Thus, denoting  $T_{ij}$  as  $T_{i(i+k)} = T_k$ , the additional constraint is that  $T_{k+1}/T_k = c$ , leading to (Tokunaga, 1978)

$$T_k = ac^{k-1}, \quad (14)$$

where  $a$  is the mean number of channels of order  $i$  that merge with one of order  $i + 1$ . A recent investigation of 408 individual networks with  $\Omega \geq 6$  in the continental United States found that the majority appeared to conform to Tokunaga self-similarity, and this was independent of  $\Omega$ . It was also found that  $a$  is relatively constant at  $a \sim 1.1$ , while  $c$  potentially reflects climatic and geologic factors  $2 \lesssim c \lesssim 3.5$  (Zanardo et al., 2013). Hence, there is significant scope for using our proposed Hölder-conditioned hypsometric triplet for summarizing landscape structure and relating this to aspects of drainage network structure such as the Tokunaga parameter,  $c$ .

### 5. Conclusion

Drawing upon classic work in geomorphology in the 1950s and 1960s that proposed the use of hypsometry as a means to analyze landscapes, and coupled to work from the 1990s on the fractal geometry of landscapes, we have developed an analysis framework based on the joint distribution function for landscape catchment area as a function of elevation and the pointwise Hölder exponents that capture the local scaling behavior of topographic roughness (Figure 3). An analysis of the conditional distributions extracted from the joint distribution in Figure 4 helps synthesize the wealth of information in Figure 3, and Strahler's original insight of using the integral of such curves can be used to produce the Hölder conditioned hypsometry,  $I_{hyp|\alpha^*}$ , and elevation-conditioned Hölder scaling profiles,  $I_{\alpha^*|z^*}$ , shown in Figure 5. Choosing to retain a direct connection to Strahler's original work, one should prioritize the former in analysis and a multivariate analysis for five different catchments from the United States shows that the best three terms to summarize the joint distribution function are the mean value for  $I_{hyp|\alpha^*}$ , that is, Strahler's original hypsometric integral,  $I_{hyp}$ , as well as the standard deviation of the values for  $I_{hyp|\alpha^*}$  around  $I_{hyp}$ , and the linear trend in  $I_{hyp|\alpha^*}$  as a function of  $\alpha^*$ . A test based on the application of an anisotropic diffusion process to the DEM for the Smoky Mountains demonstrates the utility of our approach, where a small magnitude change in the elevation values that leads to a more deeply incised valleys and sharper topographic divides is not sufficient to perturb  $I_{hyp}$  or the standard deviation of the  $I_{hyp|\alpha^*}$  but leads to a discernible change in the linear trend for  $I_{hyp|\alpha^*}$ .

As geomorphologists continue to integrate greater process knowledge into landscape evolution models, and increasingly use such tools, as well as high-resolution DEMs, to characterize landscape surfaces and the changes induced by human activity, this refined version of hypsometry that provides greater detail on the landscape elevation-roughness-area coupling should be of significant utility. In addition, because our approach renormalizes the  $z$  and  $\alpha$  values by their range, results are insensitive to a systematic shift toward an increase in the range of  $\alpha$  values as a consequence of the acquisition of higher-resolution topography. Because the estimation of pointwise Hölder exponents requires information surrounding a location, as long as topographic data are of sufficient resolution to determine the local scaling behavior accurately, then results will be robust to topographic resolution, in contrast to methods that prioritize a specific scale.

Code to undertake the analysis described in this paper, and to replicate some of the figures, is available online (at <https://github.com/ChrisKeylock/Holder-based-Hypsometry>).

## Acronyms

DEM digital elevation model  
 HECAS Hölder exponent, catchment area scaling  
 IAAWT iterated, amplitude adjusted wavelet transform  
 JPDF joint probability distribution function  
 PCA principal components analysis  
 PDF probability distribution function

## Notation

$A$  area  
 $A^*$  proportion of total area  
 $\alpha$  pointwise Hölder exponent  
 $\alpha^*$  rescaled pointwise Hölder exponent  
 $\beta$  scaling exponent  
 $c$  diffusion coefficient or Tokunaga exponent  
 $C$  scaling coefficient  
 $\delta$  small distance increment  
 $\epsilon$  probability mass function for binary variable  
 $i, j$  indices  
 $I_\alpha$  Hölder exponent, catchment area scaling (HECAS)  
 $I_{\alpha|z}$  Hölder exponent, catchment area scaling conditioned on  $z$   
 $I_{hyp}$  hypsometric integral  
 $I_{hyp|\alpha}$  hypsometric integral conditioned on  $\alpha$   
 $K$  constant  
 $N$  number of discrete intervals/number of wavelet scales  
 $\eta$  probability mass function  
 $O_{x_0 \pm \delta}$  oscillation within  $\delta$  of  $x_0$   
 $\omega$  wavelet coefficients  
 $p(\dots)$  probability distribution function  
 $P(\dots)$  cumulative distribution function  
 $r_\alpha$  departures of  $I_{\alpha|z}$  from  $I_\alpha$   
 $r_{hyp}$  departures of  $I_{hyp|\alpha}$  from  $I_{hyp}$   
 $\sigma(\dots)$  standard deviation  
 $t$  time  
 $T_{x_0}$  polynomial representing the Taylor series expansion about  $x_0$   
 $\tau$  functional relation for anisotropic diffusion  
 $\theta(\dots)$  linear trend  
 $x, y$  spatial positions  
 $X, Y$  spatial extent in two orthogonal, horizontal directions  
 $z$  elevation  
 $z^*$  rescaled elevation  
 $\mathbf{Z}$  array of elevation values

## Acknowledgments

This research was undertaken while C. K. was supported by Leverhulme Trust and Royal Academy of Engineering Senior Research Fellowship LTSRF1516-12-89. He is grateful to the Department of Aeronautics, Imperial College London, and the Department of Mechanical Engineering, Johns Hopkins University, for their hospitality during that time. E. F.-G. gratefully acknowledges support from NSF Grants EAR-1242458 (Linked Institutions for Future Earth: LIFE), EAR-1811909 (understanding deltas through the lens of their channel networks), and DMS-1839336 (data science frontiers in climate science). This work is based on data services provided by the OpenTopography Facility with support from the National Science Foundation under NSF Awards 1557484, 1557319, and 1557330. The DEMs used in this study may be accessed online (from <http://www.opentopography.org>). Specific URLs and further details regarding the field locations and the methodology are available in the supporting information.

## References

- Arneodo, A., Bacry, E., Jaffard, S., & Muzy, J. F. (1997). Oscillating Singularities on Cantor sets: A grand-canonical multifractal formalism. *Journal of Statistical Physics*, *87*, 179–209.
- Basu, S., Foufoula-Georgiou, E., Lashermes, B., & Arneodo, A. (2007). Estimating intermittency exponent in neutrally stratified atmospheric surface layer flows: A robust framework based on magnitude cumulant and surrogate analyses. *Physics of Fluids*, *19*, 115,102.
- Benzi, R., Biferale, L., Crisanti, A., Paladin, G., Vergassola, M., & Vulpiani, A. (1993). A random process for the construction of multifractal fields. *Physica D*, *65*, 352–358.
- Boon, J. D. III, & Byrne, R. J. (1981). On basin hypsometry and the morphodynamic response of coastal inlet systems. *Marine Geology*, *40*, 27–48.
- Brocklehurst, S. H., & Whipple, K. X. (2004). Hypsometry of glaciated landscapes. *Earth Surface Processes and Landforms*, *29*, 907–926. <https://doi.org/10.1002/esp.1083>
- Brozović, N., Burbank, D. W., & Meigs, A. J. (2001). Climatic limits on landscape development in the northwestern Himalaya. *Science*, *276*(5312), 571–574.

- Carson, M. A., & Kirkby, M. J. (1972). *Hillslope form and process*, (pp. 475). Cambridge, UK: Cambridge University Press.
- Chorley, R. J. (2008). The mid-century revolution in fluvial Geomorphology. In T. P. Burt, R. J. Chorley, D. Brunsten, N. J. Cox, & A. S. Goudie (Eds.), *The history of the study of landforms or the development of geomorphology, Volume 4: Quaternary and recent processes and forms (1890–1965) and the mid-century revolutions* (pp. 925–960). London: Geological Society.
- Chorley, R. J., & Kennedy, B. A. (1971). *Physical geography: A systems approach*, (pp. 370). London: Prentice-Hall International.
- Clubb, F. J., Mudd, S. M., Milodowski, D. T., Hurst, M. D., & Slater, L. J. (2014). Objective extraction of channel heads from high-resolution topographic data. *Water Resources Research*, *50*, 4283–4304. <https://doi.org/10.1002/2013WR015167>
- Evans, I. S. (1980). An integrated system of terrain analysis and slope mapping. *Zeitschrift für Geomorphologie*, *36*, 274–295.
- Evans, I. S., & McLean, C. J. (1995). The land surface is not unifractal: Variograms, cirque scale and allometry. *Zeitschrift für Geomorphologie Supplement*, *101*, 127–147.
- Furbish, D. J., & Andrews, J. T. (1984). The use of hypsometry to indicate long-term stability and response of valley glaciers to changes in mass transfer. *Journal Glaciology*, *30*(105), 199–211.
- Gagnon, J. S., Lovejoy, S., & Schertzer, D. (2003). Multifractal surfaces and terrestrial topography. *Europhysics Letters*, *62*, 801–807.
- Gagnon, J.-S., Lovejoy, S., & Schertzer, D. (2006). Multifractal Earth topography. *Nonlinear Processes in Geophysics*, *13*(5), 541–570.
- Grieve, S. W. D., Mudd, S. M., Hurst, M. D., & Milodowski, D. T. (2016). A nondimensional framework for exploring the relief structure of landscapes. *Earth Surface Dynamics*, *4*, 309–325. <https://doi.org/10.5194/esurf-4-309-2016>
- Huang, J., & Turcotte, D. L. (1989). Fractal mapping of digitized images: Application to the topography of Arizona and comparisons with synthetic images. *Journal of Geophysical Research*, *94*(B6), 7491–7495.
- Hurst, M. D., Grieve, S. W. D., Clubb, F. J., & Mudd, S. M. (2019). Detection of channel-hillslope coupling along a tectonic gradient. *Earth and Planetary Science Letters*, *522*, 30–39. <https://doi.org/10.1016/j.epsl.2019.06.018>
- INRIA (2017). <https://project.inria.fr/fraclab/>
- Jaffard, S. (1997). Multifractal formalism for functions: Parts I and II. *SIAM Journal on Numerical Analysis*, *28*, 944–998.
- Katul, G., Vidakovic, B., & Albertson, J. (2001). Estimating global and local scaling exponents in turbulent flows using discrete wavelet transformations. *Physics of Fluids*, *13*, 241–250.
- Keylock, C. J. (2003). Mark Melton's geomorphology and geography's quantitative revolution. *Transactions of the Institute of British Geographers*, *28*, 142–157.
- Keylock, C. J. (2010). Characterizing the structure of nonlinear systems using gradual wavelet reconstruction. *Nonlinear Processes in Geophysics/Nonlinear Processes in Geophysics*, *17*, 615–632.
- Keylock, C. J. (2017). Multifractal surrogate-data generation algorithm that preserves pointwise Holder regularity structure, with initial applications to turbulence. *Physical Review E*, *95*(32), 123.
- Keylock, C. J. (2019). Hypothesis testing for nonlinear phenomena in the geosciences using synthetic, surrogate data. *Earth & Space Science*, *6*, 41–58. <https://doi.org/10.1029/2018EA000435>
- Keylock, C. J., Chang, K. S., & Constantinescu, G. S. (2016). Large eddy simulation of the velocity-intermittency structure for flow over a field of symmetric dunes. *Journal of Fluid Mechanics*, *805*, 656–685.
- Keylock, C. J., Nishimura, K., & Peinke, J. (2012). A classification scheme for turbulence based on the velocity-intermittency structure with an application to near-wall flow and with implications for bedload transport. *Journal of Geophysical Research*, *117*, F01037. <https://doi.org/10.1029/2011JF002127>
- Keylock, C. J., Singh, A., & Fofoula-Georgiou, E. (2013). The influence of bedforms on the velocity-intermittency structure of turbulent flow over a gravel bed. *Geophysical Research Letters*, *40*, 1351–1355. <https://doi.org/10.1002/grl.50337>
- Kirkby, M. J. (1971). Hillslope process-response models based on the continuity equation. *Transactions of the Institute of British Geographers*, *3*, 15–30.
- Klinkenberg, B., & Goodchild, M. F. (1992). The fractal properties of topography: A comparison of methods. *Earth Surface Processes and Landforms*, *17*(3), 217–234.
- Kolwankar, K. M., & Lévy Véhel, J. (2002). A time domain characterisation of the fine local regularity of functions. *Journal of Fourier Analysis and Applications*, *8*, 319–334.
- Lashermes, B. E., & Fofoula-Georgiou, E. (2007). Area and width functions of river networks: New results on multifractal properties. *Water Resources Research*, *43*(W09405). <https://doi.org/10.1029/2006WR005329>
- Lashermes, B., Fofoula-Georgiou, E., & Dietrich, W. E. (2007). Channel network extraction from high resolution topography using wavelets. *Geophysical Research Letters*, *34*, L23S04. <https://doi.org/10.1029/2007GL031140>
- Lifton, N. A., & Chase, C. G. (1992). Tectonic, climatic and lithologic influences on landscape fractal dimension and hypsometry: Implications for landscape evolution in the San Gabriel Mountains, California. *Geomorphology*, *5*, 77–114.
- Mandelbrot, B., & van Ness, J. W. (1968). Fractional Brownian motions, fractional noises and applications. *SIAM Review*, *10*(4), 422–437.
- Milodowski, D. T., Mudd, S. M., & Mitchard, E. T. A. (2015). Topographic roughness as a signature of the emergence of bedrock in eroding landscapes. *Earth Surface Dynamics*, *3*, 483–499. <https://doi.org/10.5194/esurf-3-483-2015>
- Montgomery, D. R., & Balco, G. H. (2001). Climate, tectonics, and the morphology of the Andes. *Geology*, *29*(7), 579–582.
- Muzy, J. F., Bacry, E., & Arnéodo, A. (1993). Multifractal formalism for fractal signals: The structure-function approach versus the wavelet-transform modulus-maxima method. *Physical Review E*, *47*(2), 875–884.
- Ohmori, H. (1993). Changes in the hypsometric curve through mountain building resulting from concurrent tectonics and denudation. *Geomorphology*, *8*(4), 263–277.
- Outcalt, S. I., & Melton, M. A. (1992). Geomorphic application of the Hausdorff–Besicovich dimension. *Earth Surface Processes and Landforms*, *17*(8), 775–787.
- Passalacqua, P., Do Trung, T., Fofoula-Georgiou, E., Sapiro, G., & Dietrich, W. E. (2010). A geometric framework for channel network extraction from lidar: Nonlinear diffusion and geodesic paths. *Journal of Geophysical Research*, *115*, F01002. <https://doi.org/10.1029/2009JF001254>
- Peckham, S. D. (1995). New results for self-similar trees with applications to river networks. *Water Resources Research*, *31*(4), 1023–1029.
- Peltier, R. F., & Lévy Véhel, J. (1995). Multifractal Brownian motion: Definition and preliminary results (INRIA Report no. 2645).
- Perona, P., & Malik, J. (1990). Scale-space and edge detection using anisotropic diffusion. *IEEE Transactions on Pattern Analysis and Machine Intelligence*, *12*(7), 629–639.
- Roering, J. J., Perron, J. T., & Kirchner, J. W. (2007). Functional relationships between denudation and hillslope form and relief. *Earth and Planetary Science Letters*, *264*(1), 245–258.
- Sangireddy, H., Stark, C. P., & Passalacqua, P. (2017). Multiresolution analysis of characteristic length scales with high-resolution topographic data. *Journal of Geophysical Research: Earth Surface*, *122*, 1296–1324. <https://doi.org/10.1002/2015JF003788>
- Schreiber, T., & Schmitz, A. (1996). Improved surrogate data for nonlinearity tests. *Physical Review Letters*, *77*, 635–638.

- Seuret, S. (2006). Detecting and creating oscillations using multifractal methods. *Mathematische Nachrichten*, 279(11), 1195–1211. <https://doi.org/10.1002/mana.200510417>
- Seuret, S., & Lévy Véhel, J. (2003). A time domain characterization of 2-microlocal spaces. *Journal of Fourier Analysis and Applications*, 9, 473–495.
- Singh, A., Howard, K. B., & Guala, M. (2016). A measure of scale-dependent asymmetry in turbulent boundary layer flows: Scaling and Reynolds number similarity. *J. Fluid Mech.*, 797, 549–563. <https://doi.org/10.1017/jfm.2016.294>
- Strahler, A. N. (1952). Hypsometric (area-altitude) analysis of erosional topography. *Geological Society of America Bulletin*, 63, 1117–1142.
- Strahler, A. N. (1957). Quantitative analysis of watershed geomorphology. *EOS Transactions American Geophysical Union*, 38, 913–920.
- Strahler, A. N. (1964). Quantitative geomorphology of drainage basins and channel networks. In V. T. Chow (Ed.), *Handbook of Applied Hydrology* pp. 4–39–4–76). New York: McGraw Hill.
- Strahler, A. N. (1992). Quantitative/dynamic geomorphology at Columbia 1945–60: A Retrospective. *Progress In Physical Geography*, 16, 65–84.
- Tarboton, D. G. (1996). Fractal river networks, Horton's laws and Tokunaga cyclicity. *Journal of Hydrology*, 187, 105–117.
- Tokunaga, E. (1978). Consideration on the composition of drainage networks and their evolution. *Geographical Reports of Tokyo Metropolitan University*, 13, 1–27.
- Veneziano, D., & Iacobellis, V. (1999). Self-similarity and multifractality of topographic surfaces at basin and subbasin scales. *Journal of Geophysical Research*, 104(B6), 12,797–12,812.
- Venugopal, V., Roux, S., Foufoula-Georgiou, E., & Arneodo, A. (2006). Revisiting multifractality of high-resolution temporal rainfall using a wavelet-based formalism. *Water Resources Research*, 42, W06D14. <https://doi.org/10.1029/2005WR004489>
- Verstraeten, G., & Poesen, J. (2001). Factors controlling sediment yield from small intensively cultivated catchments in a temperate humid climate. *Geomorphology*, 40, 123–144.
- Walcott, R. C., & Summerfield, M. A. (2008). Scale dependence of hypsometric integrals: An analysis of southeast African basins. *Geomorphology*, 96, 174–186.
- Willgoose, G. R. (1994). A statistic for testing the elevation characteristics of landscape simulation models. *Journal of Geophysical Research*, 99(B7), 13,987–13,996.
- Willgoose, G. R., Bras, R. L., & Rodriguez-Iturbe, I. (1991). A physically based coupled network growth and hillslope evolution model: 1. Theory. *Water Resources Research*, 27(7), 1671–1684.
- Willgoose, G., & Hancock, G. (1998). Revisiting the hypsometric curve as an indicator of form and process in transport-limited catchment. *Earth Surface Processes and Landforms*, 23, 611–623.
- Zanardo, S., Zaliapin, I., & Foufoula-Georgiou, E. (2013). Are American rivers Tokunaga self-similar? New results on fluvial network topology and its climatic dependence. *Journal of Geophysical Research: Earth Surface*, 118, 166–183. <https://doi.org/10.1029/2012JF002392>